International Journal of Heat and Mass Transfer 52 (2009) 504–515

Contents lists available at ScienceDirect

International Journal of Heat and Mass Transfer

journal homepage: www.elsevier.com/locate/ijhmt

Neural-finite difference method (NFDM) in development of improved differential approximation (IDA) and its application for coupled conduction and radiation heat transfer in a square enclosure: An experimental validation

R.K. Mallik [a,*], S.K. Mahapatra [b,*], A. Sarkar [c]

[a] Mechanical Engineering Department, University College of Engineering Burla, 768018 Orissa, India
[b] Mechanical Engineering Department, National Institute of Technology, Rourkela, Orissa, India
[c] Mechanical Engineering Department, Jadavpur University, Kolkata, India

ARTICLE INFO

Article history:
Received 11 September 2006
Received in revised form 7 October 2007
Available online 28 July 2008

Keywords:
Improved differential approximation
Neuron model
Square enclosure
Gray participating medium
Isotropic scattering
Interferogram

ABSTRACT

The present numerical and experimental analysis addresses coupled conduction and radiation heat transfer (CCR) in differentially heated vertical isothermal walls and horizontal insulated walls of a square enclosure with absorbing, emitting and isotropic scattering participating gray medium. The P_1 approximation solution is utilized as the input signal to the neuron model. The computational domain is treated by the neural-finite difference method (NFDM) with ray tracing technique of ray emission model (REM) for the development of improved differential approximation (IDA). The output results are validated with the results of DOM. The practical implementation of IDA for wide range of radiative parameters are illustrated and examined. Experiments have been performed in a square enclosure with solid isothermal walls made of aluminum and insulated walls with bakelite, thus forming air filled cavity. Finally, the consistence of isotherm pattern of the numerical work with the interferogram captured by Mach–Zehnder interferometer corroborates the IDA theory and its realistic approach.

1. Introduction

The conduction with radiative phenomenon in a participating medium of lower opacity has been receiving considerable attention, which exists in numerous compact systems like pendrives, laptops, micro-processor chips, head lamps of foggy driving, laser therapy, etc. During operation of these devices, accumulated heat causes failure or malfunction of electronics circuits. Hence, researchers are in pursuit of a reliable CCR model for optimal design of very compact thermophysical systems.

Numerous numerical studies for one-dimensional radiation models have been reported in the literature. The researchers' reports on multi-dimensional radiation models are very few due to complexity during formulation and numerical applications. Also, most of the radiation models have neglected the conjugate mode of heat transfer in a quiescent/dynamic participating medium; which are of practical interest.

Ismail and Carlos [1] have simulated a conjugate heat transfer model for double glass window separated with 30 mm air gap and found that, for Rayleigh number 1084 the diffusive effects are prominent without convection, consequently the thermal energy interaction becomes in CCR mode. Hence, it is pertinent that, CCR mode of heat transfer prevails in a system having very compact shape and size, where the dynamics of the participating media will not be induced, because of insufficient space; hence the medium remains quiescent. Razzaque et al. [2] implemented finite element method for solving CCR mode governing equations and found convergence difficulty for very low value of wall emissivity and conduction/radiation parameter, but claimed robustness for simulation of very low opacity without reporting the results. Kim and Baek [3] examined the CCR model only for overall optical thickness 0.1, 1.0 and 5.0 for non-scattering medium only. Sakami et al. [4] investigated a new approach of DOM for the CCR problem in a semitransparent medium for two-dimensional complex enclosures without considering the very low overall optical thickness (<0.20). Yuen and Takara [5] studied the CCR problem in a rectangular enclosure for non-scattering medium for overall optical thickness 0.1, 0.5, 1.0, 2.0 and 5.0, but clearly not mentioned the practical application of diffusion approximations. Mishra et al. [6] formulated the DOM approach to the collapse dimension method (CDM) for producing faster results because of not considering the solid angle, but not mentioned the physical significance of

* Corresponding authors. Address: University College of Engineering, Mechanical Engineering Department, Qrs. No. 3R/4, Professor Colony, Burla Engineering College Campus, 768018 Orissa, India. Tel.: +91 9861048277/+91 9437257967; fax: +91 6632430204.
E-mail addresses: ramesh_mallik@yahoo.com (R.K. Mallik), swarupkumar_m@yahoo.com (S.K. Mahapatra).

0017-9310/$ - see front matter © 2008 Elsevier Ltd. All rights reserved.
doi:10.1016/j.ijheatmasstransfer.2008.04.073

Nomenclature

A_1	linear anisotropic scattering factor
AR	aspect ratio (H/L)
F_{i-j}	view factor from source (i) to a receiver (j)
G	irradiation (W/m^2)
g	dimensionless irradiation
I, $\bar{I}$	radiation intensity [W/m^2], dimensionless radiative intensity
I_b	black body radiation intensity ($=\sigma T^4/\pi$) [W/m^2]
k	thermal conductivity [W m^{-1} K^{-1}]
L	characteristic length [m]
$\vec{q}_r$, $\vec{q}_c$	radiation and conduction heat flux vector [W/m^2]
q_r, q_c	non-dimensionalised radiation and conduction heat flux vector
QR	total radiative heat flux
QC	total conductive heat flux
RC	radiation–conduction parameter $\left(=\frac{\sigma T_H^3 L}{k}\right)$
$\vec{r}$	location of a domain with direction
S	distance of a discrete surface to another sub-surface
$\dot{S}$	ODA source
S_r	representative source
$\bar{S}$	average thickness of a radiation element
s_0	geometrical distance of a representative source
$\hat{s}$	direction of propagation of radiation intensity
T	absolute temperature [K]
T_H, T_C	hot and cold wall temperatures [K]
X, Y	dimensionless co-ordinate

Greek symbols

α_a	absorption coefficient [1/m]
α_s	scattering coefficient [1/m]
α	thermal diffusivity [m^2/s]
β	total extinction coefficient ($\alpha_a + \alpha_s$) [1/m]
Ω	solid angle [Sr]
ω	single scattering albedo $\left(\frac{\alpha_s}{\beta}\right)$
σ	Stefan–Boltzmann's constant $\left(5.67 \times 10^{-8}\ \text{W m}^{-2}\ \text{K}^{-4}\right)$
ε	wall emissivity
τ	total optical depth (βL)
θ	dimensionless temperature $\left(\frac{T}{T_H}\right)$
δ_{ij}	Kronecker delta

Subscripts

H, C and b hot, cold and bottom wall, respectively
w, m, t, c, h wall, medium, top, cold, hot

modified CDM. In the group of integral methods, the discrete transfer methods (DTM) have attracted considerable attention in recent years. Shih and Chen [7] have proposed a discretised intensity method for two-dimensional system with enclosing radiative and conductive media, in which the two-dimensional effect of radiative flux is not taken into consideration. Coelho and Carvalho [8] have implemented conservative formulation of the DTM in two- and three-dimensional participating medium with energy conservation in CCR mode with absorption coefficient of medium 0.25, 0.5 and 1 m^{-1} only. Raithby and Chui [9] developed a finite-volume method that uses the same non-orthogonal boundary fitted mesh as methods for computing fluid flow and convective heat transfer. Modest [10] and Olfe [11] have tackled the ray effect, i.e. descretisation of the angular distribution of intensity by breaking up the radiation intensity into two parts: the intensity due to medium and the intensity due to enclosure wall, which leads to modified discrete ordinate method (MDO) [12,13].

Deterministic methods can deal with anisotropic scattering by means of spherical harmonics method (SHM), i.e. P_N-approximation. Higher order SHM can also predict stellar radiance from distant stars. However, higher order formulation is quite exhaustive, because of mathematical complexity arises during formulation of PDEs. But, P_1 formulation is quite easy and popular because of its grid compatibility. The P_1 results can be modified and improved by modified differential approximation (MDA)[10] and improved differential approximation (IDA), respectively, for optically thin medium without pursuing higher order P_N approximation. Ratzel and Howell [14] and Bayazitoglu et al. [15] had formulated P_3 approximation for radiative mode only and examined better results for lower optical thickness (>0.5). The P_1 model should typically be used for optical thickness >1. But for optical thickness $\gg$1, P_1 and Rosseland models are best alternatives as implemented in Fluent Software [16]. For optically thin problems,instead of higher order SHM, only the REM [17], MDA [10,18], IDA [19] are appropriate and compatible for multi-dimensional domain.

Mahapatra et al. [20] had simulated CCR model using DOM for optical thickness 0.2, 1 and 2, and found lack of accuracy for higher values. The same remarks had also been cited by Fiveland [21]. But for lower optical thickness (<0.2) the convergence is not entertained [2]. Mahapatra et al. also developed hybrid model [22] by blending P_1 approximation with DOM, but encountered the same problem for optical thickness below 0.1. Although, the DOM is more accurate for optically thin or moderately thick medium, but for lower overall opacity (<0.1) the numerical results are not reported by many researchers.

The analysis of radiation heat transfer using the radiation element method by ray emission model (REM) [17], which is a generalized numerical method for calculating radiation heat transfer between absorbing, emitting and scattering media and specular or diffuse surface with arbitrary three-dimensional configurations, explains the average optical path of the ray. This concept of ray tracing has been utilized in the present work, with NFDM for developing the numerical code of a realistic CCR model.

1.1. Present work

The present work is an attempt to implement the virtues of REM and IDA, with the underlying principle of neuron model (Appendix) for simulation of very low overall optical thickness (0.0001) to optically thick (5.0) in a two-dimensional enclosure. The P_1 approximation over predicts the domain temperature 5% more [23], but after implementing the present model this has been reduced.

Fortunately, the gray behavior of atmospheric gases, i.e. a mixture of diatomic O_2, N_2, linear tri-atomic gas CO_2, non-linear tri-atomic gas H_2O, etc., in 296 K are more or less justified [24]. Furthermore, the absorption of the gases in far/near infra-red region is in bound–bound region with lower energy state. Although, the assumption of gray nature of the domain is not realistic, but Modak [25] explained and justified in his work that the gray gas and isothermal assumption yields accurate predictions of heat flux in small to moderate size domain but not for large size domain. This prompts the authors to assume the gray property of air during simulation of the experimental domain. Han and Baek [26] have also simulated the natural convection phenomena affected by radiation in cylindrical annuli for non-scattering air with extinction coefficient 0.3 with gray behavior of air and the isotherms are compared with the experiments of Kuehn and Goldstein [27]. But, no experimental validation of CCR model has been reported till date, as far as authors' knowledge is concerned.

The intent of the experimental investigation is to demonstrate the practical implementation of the present CCR model in a square enclosure with air in cavity. The consistence of isotherm patterns of numerical results with the interferogram, i.e. experimental contours is discussed and illustrated.

The major thesis of this paper is that, the CCR model may be simulated for any justified range of conductive and radiative properties of medium and wall. Also, the practical application of this model has been illustrated along with validation of numerically obtained isotherms with interferograms. This happens, because of the efficiently applied NFDM concept during simulation of the CCR model.

1.2. Experimental procedure

The purpose of the experiment was to capture the interferogram by Mach–Zehnder interferometer of the physical domain ($10 \times 10 \times 250$ mm) with quiescent air as shown in Fig. 3(a) by the way the CCR heat transfer through the participating medium is assessed and visualized.

The detailed of the experimental set up is shown in Fig. 3(c). The schematic diagram of the test cell used for the experiment is shown Fig. 3(b). The test cell is made of two vertical isothermal walls made of polished aluminum and the two horizontal walls are bakelite. The bakelite walls are placed above and below the projected portions of the hot and cold baths as shown in Fig. 3(b). The length of the test domain is taken as 250 mm. The compensating cell was fabricated without the hot and cold bath for the purpose of maintaining the same optical path length of the laser beam. At the front and back of the test and compensating cell, optical quality glass windows of 0.9 mm thick, were installed for interferometric measurement.

A 35 mW, continuous wave ($\lambda = 632.8$ nm) He–Ne laser is employed as the coherent light source for the interferometer. The original laser beam is of 1 mm diameter. A spatial filter is required to expand the beam to any convenient size. In the present experiment, the expanded beam diameter is 20 mm. This expanded beam is splitted by a beam splitter and one part is passed through the test cell and other part is passed through the compensating cell after reflection through a mirror as shown in Fig. 3(c). Again the test cell beam is reflected by mirror and projected to the second beam splitter near the screen. The two beams now produce interference and the fringes are seen on the screen when the beams are aligned [28]. A CCD (charged coupled device) camera of spatial resolution 768×576 pixel has been used to capture the interferometric images. The CCD camera is connected to PC based image processing system through an 8 bit A/D card.

During the experiment the entire experimental set up was mounted on four pneumatic isolation mounts, for the purpose of nullifying the vibration occurred during the flow of hot and cold oil from the refrigeration unit and the air compressor. Both the hot and cold bath units and air compressor are kept away from the set up to avoid the ground vibration. This stabilizes the interferometric images and facilitates better image acquisition. Finally, after 4 h the steady state was reached. The fringe pattern was captured by the CCD camera as shown in Fig. 11. This set up has been developed by DST, India sponsored project.

The details of the numerical simulation of this physical domain are discussed during the validation of the present CCR model.

2. Mathematical analysis

The computational domain is shown with boundary conditions in Fig. 1. The surfaces enclosing the gray medium are diffusely emitting radiative energy. (See Fig. 2.)

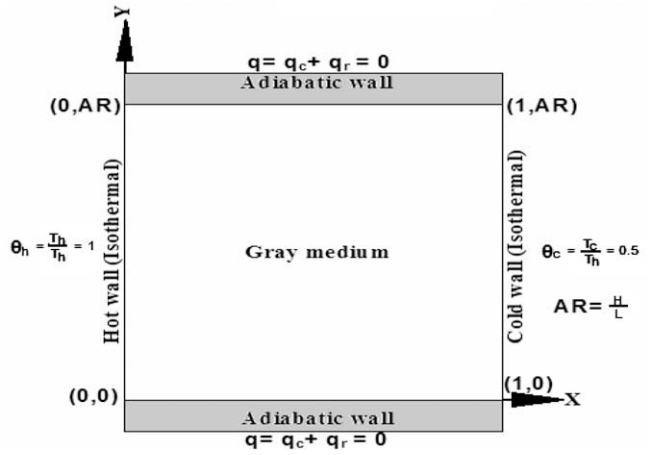

Fig. 1. Computational test domain.

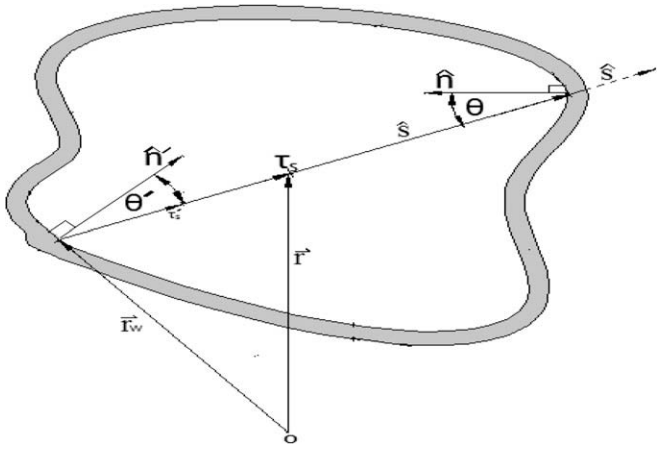

Fig. 2. Radiative intensity within an arbitrary enclosure.

The radiative transport equation (RTE) in an optical co-ordinates is given by

$$\hat{s}\cdot\nabla_\tau I + I = (1-\omega)I_b + \frac{\omega}{4\pi}\int_{4\pi} I(\hat{s})\Phi(\hat{s}\cdot\hat{s}')\,d\Omega', \tag{1}$$

where $\hat{s}$ and $\hat{s}'$ represent the out going and incoming direction, respectively, $d\Omega'$ represents the solid angle.

In a gray medium with uniform absorptivity, scattering and with $\Phi(\hat{s},\hat{s}') = 1$ Eq. (1) can be reduced to:

$$\hat{s}\cdot\nabla_\tau I + I = (1-\omega)I_b + \frac{\omega}{4\pi}\int_{4\pi} I(\hat{s})\,d\Omega'. \tag{2}$$

From the definition of irradiation, i.e. radiance approaching a location 'r' from all direction yields the formulae:

$$G(\vec{r}) = \int_{4\pi} I(\vec{r},\hat{s})\cdot d\Omega, \tag{3}$$

where $\hat{s} = \sin\theta\cdot\cos\phi\cdot\hat{i} + \sin\theta\cdot\sin\phi\cdot\hat{j} + \cos\theta\cdot\hat{k}$

$$d\Omega = \frac{dA}{r^2} = \frac{r\sin\theta\cdot d\phi\cdot r d\theta}{r^2} = \sin\theta\cdot d\theta\cdot d\phi.$$

For the integration, the polar angle θ varies from 0 to π and azimuthal angle ϕ varies from 0 to 2π, now integrating for the said limits:

$$\int_{4\pi} d\Omega = 4\pi, \quad \int_{4\pi}\hat{s}\cdot d\Omega = 0,$$
$$\int_{4\pi}\hat{s}\hat{s}d\Omega = \frac{4\pi}{3}\delta_{ij}, \quad \text{and} \quad \int_{4\pi}\hat{s}\hat{s}\hat{s}d\Omega = 0.$$

The radiative flux in a particular direction $\hat{s}$ is a vector quantity which is defined as

$$\vec{q}(\vec{r}) = \int_{4\pi} I(\vec{r},\hat{s})\cdot\hat{s}\,\mathrm{d}\Omega. \tag{4}$$

Now taking zeroth moment of Eq. (2) and integrating over the solid angle becomes:

$$\nabla_\tau\cdot\vec{q} = (1-\omega)(4\pi I_\mathrm{b} - G). \tag{5}$$

Taking the first moment of the equation, i.e. multiplying $\hat{s}\mathrm{d}\Omega$ and integrating over all solid angles:

$$\begin{aligned}&\frac{1}{4\pi}\nabla_\tau\cdot\left[G\int_{4\pi}\hat{s}\hat{s}\,\mathrm{d}\Omega + 3\vec{q}\cdot\int_{4\pi}\hat{s}\hat{s}\hat{s}\,\mathrm{d}\Omega\right]\\ &\quad+\frac{1}{4\pi}\left[G\int_{4\pi}\hat{s}\,\mathrm{d}\Omega + 3\vec{q}\cdot\int_{4\pi}\hat{s}\hat{s}\,\mathrm{d}\Omega\right]\\ &\quad\cong(1-\omega)I_\mathrm{b}\int_{4\pi}\hat{s}\,\mathrm{d}\Omega+\frac{\omega}{4\pi}G\int_{4\pi}\hat{s}\,\mathrm{d}\Omega.\end{aligned} \tag{6}$$

For integral of any odd multiple of $\hat{s}$ is reduces to zero.

Eq. (6) takes the form as

$$\begin{aligned}&\tfrac{\nabla_\tau\cdot G\delta_{ij}}{3}+\vec{q}\delta_{ij}=0\\ &\Rightarrow\vec{q}=-\tfrac{\nabla_\tau G}{3}.\end{aligned} \tag{7}$$

It is quite evident from the above equation that the negative gradient of irradiation gives the radiative heat flux. By substituting Eq. (7) in Eq. (5) the irradiation transport equation is deduces as follows:

$$\nabla_\tau^2 G - 3(1-\omega)G = -3(1-\omega)4\pi I_\mathrm{b}. \tag{8}$$

The P_1 approximation governing equations and boundary conditions are transformed after utilizing non-dimensional variables as follows:

$$\theta=\frac{T}{T_\mathrm{H}};\ X=\frac{x}{L};\ Y=\frac{y}{H};\ \mathrm{AR}=\frac{H}{L};\ \mathrm{RC}=\frac{\sigma T_\mathrm{H}^3 L}{k};\ g=\frac{G}{\sigma T_\mathrm{H}^4}$$

$$\tau=\beta L;\ \bar{I}_\mathrm{b}=\frac{I_\mathrm{b}}{\sigma T_\mathrm{H}^4};\ q_\mathrm{c}=\frac{\vec{q}_\mathrm{c}}{kT_\mathrm{H}/L};\ q_\mathrm{r}=\frac{\vec{q}_\mathrm{r}}{kT_\mathrm{H}/L}.$$

The energy conservation equation for steady state without heat generation and considering the quiescent medium:

$$-k\nabla^2 T+\nabla\vec{q}_\mathrm{r}=0. \tag{9}$$

Now for two-dimensional domain the energy equation becomes:

$$-k\left(\frac{\partial^2 T}{\partial x^2}+\frac{\partial^2 T}{\partial y^2}\right)+(1-\omega)(4\pi I_\mathrm{b}-G)=0. \tag{10}$$

The energy equation in the non-dimensional form is expressed here under:

$$\frac{\partial^2\theta}{\partial X^2}+\frac{1}{\mathrm{AR}^2}\frac{\partial^2\theta}{\partial Y^2}=\tau(1-\omega)\cdot\mathrm{RC}[4\theta(r)^4-g(r)]. \tag{11}$$

The boundary conditions for the energy equation are given as

(i) for the hot wall $\theta(0,Y)=1$ for $0\leqslant Y\leqslant \mathrm{AR}$
(ii) for the cold wall $\theta(1,Y)=\left(\frac{T_\mathrm{C}}{T_\mathrm{H}}\right)=0.5$ for $0\leqslant Y\leqslant \mathrm{AR}$
(iii) for the bottom adiabatic wall $\vec{q}_\mathrm{c}+\vec{q}_\mathrm{r}=0$ for $Y=0$ and $0\leqslant X\leqslant 1$
(iv) for the top adiabatic wall $\vec{q}_\mathrm{c}+\vec{q}_\mathrm{r}=0$ for $Y=\mathrm{AR}$ and $0\leqslant X\leqslant 1$.

In the P_1 approximation the non-dimensionalised Irradiation transport equation appears as

$$\frac{1}{\tau^2}\left(\frac{\partial^2 g}{\partial X^2}+\frac{\partial^2 g}{\mathrm{AR}^2\partial Y^2}\right)-(1-\omega)(3-A_1\omega)g = -(1-\omega)(3-A_1\omega)4\theta^4. \tag{13}$$

The boundary conditions (BCs) for all the four walls of the enclosure requires the emanating radiative heat flux from the walls as expressed here under

$$\vec{q}_\mathrm{r}=-\frac{1}{3-A_1\omega}\nabla_\tau G, \tag{14}$$

which depicts the gradient of irradiation at walls.

The wall boundary conditions as derived by the present method is

$$2\vec{q}_\mathrm{r}\cdot\hat{n}=\frac{\varepsilon}{2-\varepsilon}(4\pi I_\mathrm{b}-G). \tag{15}$$

By combining the above two equations, the following boundary condition equation is derived, which is more compatible for the treatment of boundary:

$$-\frac{2-\varepsilon}{\varepsilon}\times\frac{2}{3-A_1\omega}\times(\hat{n}\cdot\nabla_\tau G)+G=4\pi I_\mathrm{bw}. \tag{16}$$

After non-dimensionalisation the boundary conditions are:

$$(-1)^i\frac{2-\varepsilon}{\varepsilon}\frac{2}{3-A_1\omega}\frac{\partial g}{\partial X_i}+\tau g=4\tau\theta_i^4 \tag{17}$$

for $i=1, 2, 3, 4$ hot, cold, bottom and top wall, respectively.

2.1. Improved differential approximation formulation

The equation of transfer with radiative source along a pencil of ray emanating from wall and source in a particular direction $\hat{s}$, the intensity at a particular location and directed from r' to r can be presented,

$$\frac{\mathrm{d}I(\vec{r},\hat{s})}{\mathrm{d}\tau}+I(\vec{r},\hat{s})=S(\vec{r},\hat{s}). \tag{18}$$

This equation is linear differential equation commonly known as Leibnitz's linear equation, which can be solved by implementing the boundary condition at the wall, $J_\mathrm{w}=J_\mathrm{w}(\vec{r}');\tau=\tau_\mathrm{s}';S=0$; the equation becomes after putting BCs

$$I(\vec{r},\hat{s})=\frac{J_\mathrm{w}}{\pi}(\vec{r}').\mathrm{e}^{-\tau_\mathrm{s}}+\int_0^{\tau_\mathrm{s}}S(\vec{r}'+s'\hat{s},\hat{s})\cdot\mathrm{e}^{-(\tau_\mathrm{s}-\tau_\mathrm{s}')}\,\mathrm{d}\tau_\mathrm{s}'. \tag{19}$$

In IDA the medium related intensity is

$$I_\mathrm{m}(\vec{r},\hat{s})\approx\int_0^{\tau_\mathrm{s}}S^*(\vec{r}'+s'\hat{s},\hat{s})\cdot\mathrm{e}^{-(\tau_\mathrm{s}-\tau_\mathrm{s}')}\,\mathrm{d}\tau_\mathrm{s}', \tag{20}$$

where

$$\dot{S}(\vec{r},\hat{s})=(1-\omega)\dot{I}_\mathrm{b}(r)+\frac{\omega}{4\pi}\dot{G}(r). \tag{21}$$

Dot above the variables are adapted for distinguishing ODA variables.

Hence forth the ODA source as in Eq. (21) may be introduced as follows for improvement of medium intensity

$$I_\mathrm{m}(\vec{r},\hat{s})\approx\int_0^{\tau_\mathrm{s}}\dot{S}(\vec{r}'+s'\hat{s},\hat{s})\cdot\mathrm{e}^{-(\tau_\mathrm{s}-\tau_\mathrm{s}')}\,\mathrm{d}\tau_\mathrm{s}'. \tag{22}$$

The source term is approximated as

$$S(\vec{r}+s'\hat{s},\hat{s}) \approx \dot{S}(\vec{r},\hat{s}) - (\tau_s - \tau'_s)\frac{d\dot{S}(\vec{r},\hat{s})}{d\tau_s}$$
$$I_m(\vec{r},\hat{s}) \approx \int_0^{\tau_s}\left[\dot{S}(\vec{r},\hat{s}) - (\tau_s-\tau'_s)\frac{d\dot{S}(\vec{r},\hat{s})}{d\tau_s}\right]e^{-(\tau_s-\tau'_s)}d\tau'_s$$
$$\Rightarrow I_m \approx \int_0^{\tau_s}\left[\dot{S} - (\tau_s-\tau'_s)\frac{d\dot{S}}{d\tau_s}\right]e^{-\tau_s+\tau'_s}d\tau'_s. \quad (23)$$

Here, the τ_s and τ'_s are of same meaning in a gray medium and $\frac{\tau'_s}{\tau_s}$ = numerical value and the double derivative of a linear function is zero. Now Eq. (23), which is a definite integral can be presented as

$$I_m \approx \int_0^{\tau_s}\dot{S}\cdot e^{-\tau_s+\tau'_s}d\tau'_s - \int_0^{\tau_s}\tau_s\frac{d\dot{S}}{d\tau_s}e^{-\tau_s+\tau'_s}d\tau'_s + \int_0^{\tau_s}\tau'_s\frac{d\dot{S}}{d\tau_s}e^{-\tau_s+\tau'_s}d\tau'_s.$$

Now integrating by parts and considering the limits:

$$I_m \approx \dot{S} - \dot{S}e^{-\tau_s} - \tau_s\frac{d\dot{S}}{d\tau_s} + \tau_s e^{-\tau_s}\frac{d\dot{S}}{d\tau_s} + \tau_s\frac{d\dot{S}}{d\tau_s} - \frac{d\dot{S}}{d\tau_s} + e^{-\tau_s}\frac{d\dot{S}}{d\tau_s}$$
$$\Rightarrow I_m \approx \dot{S}(1-e^{-\tau_s}) - (1-(1+\tau_s)e^{-\tau_s})\frac{d\dot{S}}{d\tau_s}. \quad (24)$$

Now for elimination of the differential term the following mathematical treatments are:

$$I_m \approx (1-e^{-\tau_s})\left[\dot{S} - \frac{d\dot{S}}{d\tau_s}\left(1 - \frac{\tau_s e^{-\tau_s}}{1-e^{-\tau_s}}\right)\right]. \quad (25)$$

Now, considering the coefficient of differential in Eq. (25) as the optical thickness

$$\tau_0 = \left(1 - \frac{\tau_s e^{-\tau_s}}{1-e^{-\tau_s}}\right) = \beta s_0$$
$$\Rightarrow \tau_0 = \int_0^{s_0}\beta(\vec{r}-s''\hat{s})\,ds'', \quad (26)$$

where $0 < \tau_0 < (1, \tau_s)$ and the s'' is the distance from $\vec{r}$ into $-\hat{s}$. Now Eq. (24) may be expressed as

$$I_m \approx \dot{S}(\vec{r}-s_0\hat{s},\hat{s})(1-e^{-\tau_s})$$
$$\Rightarrow I_m \approx S_r(1-e^{-\tau_s}). \quad (27)$$

The opaque wall radiosites are given as

$$J_w(\vec{r}) = \varepsilon\pi I_{bw}(\vec{r}) + (1-\varepsilon)\int_{\hat{s}\cdot\hat{n}<0} I(\vec{r},\hat{s})|\hat{s}\cdot\hat{n}|d\Omega. \quad (28)$$

This equation again can be solved by standard surface transport method, such as small zones, to give:

$$J_i = \varepsilon_i\pi I_{bi} + (1-\varepsilon_i)\sum_{j=1}^{N}[J_j e^{-\tau_{ij}} + \pi S^*_{ij}(1-e^{-\tau_{ij}})]F_{i-j,i=1,2,3\ldots N}. \quad (29)$$

Once the radiosites are known, the improved values for incident radiation and radiative heat flux any where inside the medium follow from their definition,

$$G(\vec{r}) = \frac{1}{\pi}\int_{4\pi}[J_w(\vec{r})\cdot e^{-\tau_s} + \pi S_r\cdot(1-e^{-\tau_s})]d\Omega$$
$$= \int_A [J_w(\vec{r}')\cdot e^{-\tau_s} + \pi S_r\cdot(1-e^{-\tau_s})]\frac{\cos\theta'\,dA}{\pi S^2} \quad (30)$$

$$\vec{q}(\vec{r}) = \frac{1}{\pi}\int_{4\pi}[J_w(\vec{r})e^{-\tau_s} + \pi S_r(1-e^{-\tau_s})]\hat{s}\,d\Omega$$
$$= \int_A [J_w(\vec{r}')e^{-\tau_s} + \pi S_r(1-e^{-\tau_s})]\hat{s}.\frac{\cos\theta'\,dA}{\pi S^2}. \quad (31)$$

The average optical thickness as explained by ray emission model (REM) Maruyama [17]. The following average thickness $\bar{S}$ of the radiation element in the direction $\hat{s}$ has been calculated as follows:

$$\bar{S} = \frac{V}{A(\hat{s})}, \quad (32)$$

where V is the volume of the tetrahedron through which the ray travels from a sub-node to the node.

A $(\bar{s})$ is the area projected on to the surface normal to $(\bar{s})$ direction of propagation of the ray. The average optical path of a ray is defined as

$$\tau_s = \beta\bar{S}. \quad (33)$$

The calculation of solid angles along with the wall intensity and the medium related intensity from the discrete surfaces to the other nodes are calculated by implementing the equations as cited by Sakami et al. [12,13].

3. Numerical procedure

The finite deference method (FDM) is implemented during solving the purely conductive energy equation by SOR method and finally the solution is converged with due accuracy ($\theta^{m+1} - \theta^m < 10^{-8}$). The FDM scheme utilized 5-node technique in the domain and image node technique at the insulated walls. This temperature field after the solution of purely conductive energy equation is utilized as the initial guess temperature field for the CCR heat transfer energy equation, which is solved by Newton–Raphson method because of the presence of radiative heat flux (i.e. with θ^4 expression) with non-linearity in character. Now the irradiation transfer equation is solved by utilizing the temperature field out put of Newton–Raphson method with a SOR type of sweep with convergence criteria ($g^{m+1} - g^m < 10^{-7}$). After getting an irradiation field both the energy equation and irradiation equations are coupled in a loop having convergence criteria ($\theta^{m+1} - \theta^m < 10^{-8}$) of the temperature field where $(m+1)$ means the new and 'm' means the previous value during the iteration. In this way the numerical solution of the RTE is worked out by P_1 approximation method. The temperature and irradiation at each node of the computational domain is delivered as the input signals defined in a model of neuron. The detail of the model of neuron is discussed with its compatibility to solve the radiation models [29,30] (Appendix).

Now the ODA source is calculated by Eq. (21). As in Eq. (27) the representative value of the source (S_r) at each node corresponding to other sub-nodes is enumerated with the direction of location of the sub-node by linear interpolation method (back tracking the ODA source). This generates a global matrix of order 1681×1681 for improved representative source values.

The average optical path length from each node to other (one to one correspondence) is calculated by ray emission model technique explained in [17]. The global view factor matrix is generated by utilizing Hottel's cross string method and the corner surface view factors are calculated by employing contour integration technique. The improved wall radiosites are calculated by implementing standard surface transport method with small zones.

The global solid angle matrix is generated by considering the wall as very small zones and the medium as very small cells having two orthogonal intersecting planes at the nodal point.

After arriving the improved solution, it was observed the rounding of error was eminent which is minimized after utilizing intelligent use of activation function as defined and explained in the model of neuron [29,30] and Appendix. The improved irradiation matrix is utilized and the energy equation is solved without any relaxation factor (i.e. accepting the fresh values in each sweep) with a few number of iterations as cited by Modest [19] without entering a loop for convergence. The performance and efficiency

of IDA with NFDM and experimental validation along with the radiative properties of medium and wall are discussed in the following section.

4. Results and discussion

Now, the effect of wall and medium properties on the isotherm contours and the heat transfer is investigated along with the procedures to simulate the present CCR model for practical/experimental domains.

Table 1
Grid independent test (RC = 10, $\tau = 1$, $\omega = 0.5$, $\varepsilon = 0.5$, $\theta_H = 1$ and $\theta_C = 0.5$)

Grid	QCH	QRH	QCC	QRC	QCb	QRb	θ_{center}
21×21	1.1443	2.7996	1.6509	1.9156	0.1200	−0.1345	0.8113
31×31	1.1686	2.7323	1.7132	1.9344	0.1231	−0.1371	0.8172
41×41	1.1763	2.6998	1.7436	1.9452	0.1222	−0.1374	0.8195
45×45	1.1721	2.7689	1.7965	2.0621	0.1234	−0.1354	0.8198
51×51	1.1708	2.7708	1.7982	2.0710	0.1236	−0.1321	0.8200

4.1. Grid independent test

The grid independent test is depicted in Table 1 in order to visualize the effect of grid size on the results. It is observed during simulation of this model from lower size grid to higher size grid that the computational time hikes drastically. From Table 1 the grid size 41×41 is selected for all the simulations to contemplate the accuracy and reliability of results with viable computational expenses.

4.2. Effect of radiative parameters

To visualize and characterize the effect of each parameter on the phenomenon, it is required to vary one parameter by keeping other parameters constant. The results of both IDA and ODA are presented and compared.

4.2.1. Effect of optical thickness (τ)

The radiative heat transfer dominates at lower opacity as depicted in the Fig. 4 and Tables 2 and 3. As the value of opacity increases, it substantially improves the absorption and out scattering, which attenuates the radiative intensity.

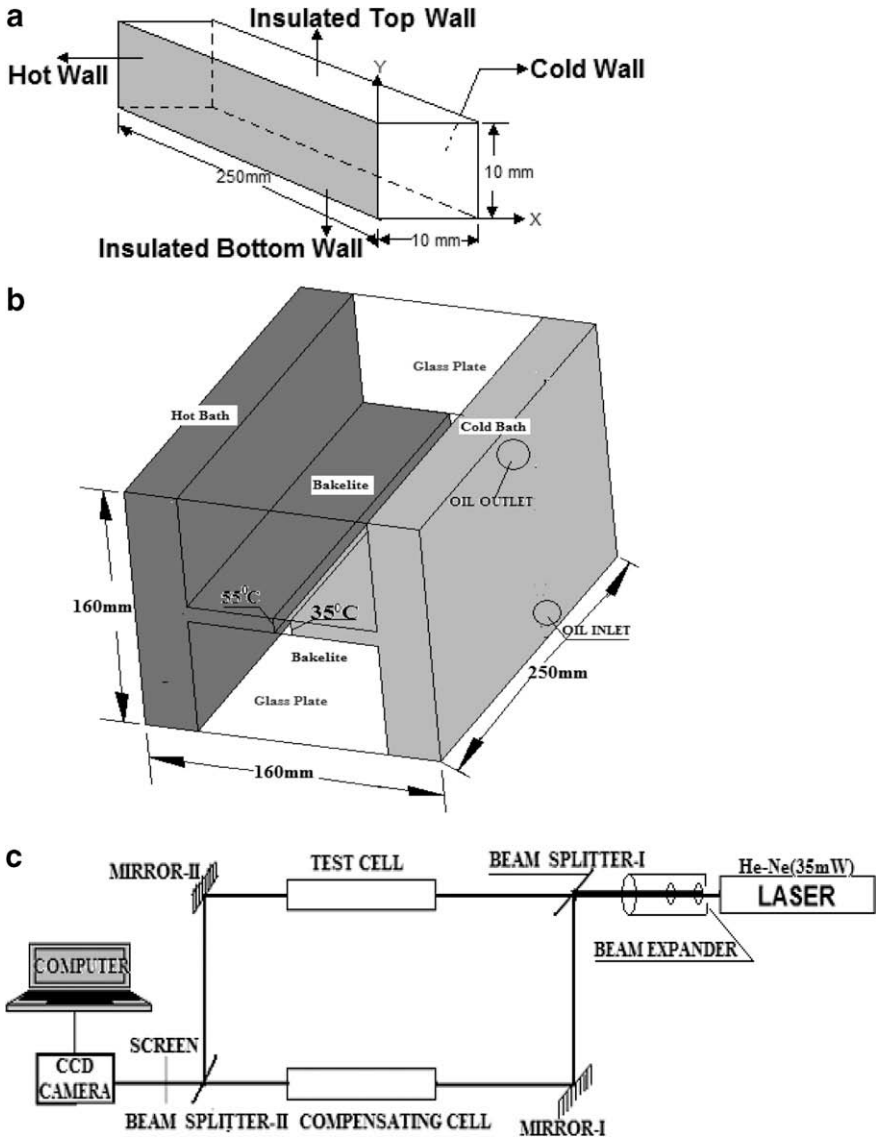

Fig. 3. Schematic diagrams of experimented cavity (a), experimental setup (not to scale) (b), Mach–Zehnder interferometer (c).

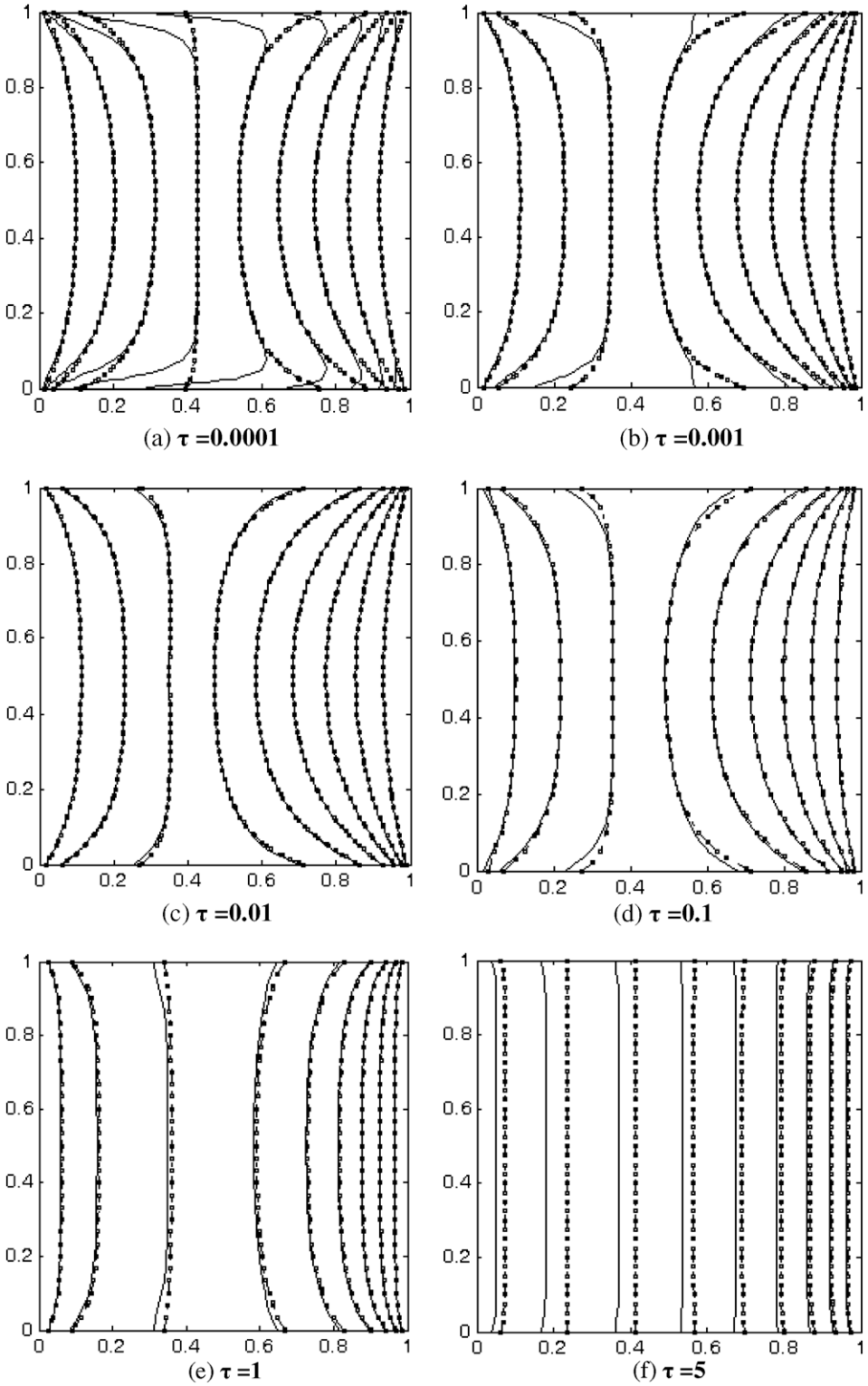

Fig. 4. Comparison of isotherm patterns of ODA (▫▫▫) and IDA (—) at different opacities. When (RC = 10, $\omega = 0.5$, $\varepsilon = 0.5$).

The effect of the insulated walls on the isotherm patterns are depicted in Fig. 4(a), (b) and (c) for IDA model. Fig. 5 depicts the central non-dimensional temperature for different values of opacity and compared with DOM CCR model [20].Many CCR model researchers have not reported results for optically thin ($\ll 1$) medium, except Razzaque et al. [2], as other models break down for this range [2].

4.2.2. Effect of radiation–conduction parameter (RC)

As the RC value is varied from zero to 100, a significant change in isotherm patterns for both ODA and IDA are observed in Fig. 6. For higher value of RC, the more bent isotherms illustrate the dominance of radiation heat transfer. Fig. 6(d) demonstrates intense heating of insulated walls, as the heat flux will not be carried away through these walls.

Table 2
IDA

Constant variables	Variable changed	QCH	QRH	QCC	QRC	QCb	QRb	θ_{center}
RC = 10, ω = 0.5, ε = 0.5	τ = 0.0001	0.9977	6.5075	0.7629	0.244	−1.474	1.4081	0.7674
	τ = 0.001	0.7484	3.7766	1.1318	2.5086	0.0789	−0.1033	0.7848
	τ = 0.01	0.7290	3.4575	1.1815	2.811	0.2238	−0.2522	0.7875
	τ = 0.1	0.8003	3.3664	1.1284	2.7393	0.2152	−0.2478	0.7967
	τ = 0.2	0.8704	3.288	1.3785	2.638	0.1971	−0.2262	0.8037
	τ = 1	1.1763	2.6998	1.7436	1.9452	0.1222	−0.1374	0.8195
	τ = 2	1.2736	2.185	1.801	1.3651	0.0795	−0.0902	0.8193
	τ = 5	1.2634	1.3638	1.5469	0.5986	0.0281	−0.0378	0.8119
τ = 1, ω = 0.5, ε = 0.5	RC = 0.0	0.5000	0.0000	0.5000	0.0000	0.0000	0.0000	0.7500
	RC = 0.01	0.5010	0.0028	0.5022	0.0016	0.0002	−0.0002	0.7502
	RC = 0.1	0.5099	0.0280	0.5215	0.0157	0.0024	−0.0023	0.7524
	RC = 1.0	0.5958	0.2767	0.6984	0.1654	0.0217	−0.0214	0.7698
	RC = 10.0	1.1763	2.6998	1.7436	1.9452	0.1222	−0.1374	0.8195
	RC = 40.0	2.1084	10.935	3.2902	8.3755	0.2377	−0.3588	0.8191
	RC = 100.0	3.2240	27.9677	4.7412	21.11	0.6792	−0.0081	0.8175
τ = 1, RC = 10, ε = 0.5	ω = 0.0	1.5248	2.7006	2.1198	1.8099	0.0948	−0.1048	0.8194
	ω = 0.5	1.1763	2.6998	1.7436	1.9452	0.1222	−0.1374	0.8195
	ω = 1.0	0.6362	2.7021	1.0465	2.1813	0.2158	−0.2477	0.7851
τ = 1, RC=10, ω = 0.5	ε = 0.1	1.3625	0.5613	1.5322	0.3242	0.0149	−0.0128	0.7953
	ε = 0.5	1.1763	2.6998	1.7436	1.9452	0.1222	−0.1374	0.8195
	ε = 1.0	0.9607	5.6722	1.7035	4.4127	0.2174	−0.3494	0.8296

Table 3
ODA

Constant variables	Variable changed	QCH	QRH	QCC	QRC	QCb	QRb	θ_{center}
RC = 10, ω = 0.5, ε = 0.5	τ = 0.0001	0.8389	4.0474	1.0209	2.431	0.0947	−0.1917	0.7674
	τ = 0.001	0.7215	3.5588	1.1761	2.9177	0.2336	−0.2339	0.7848
	τ = 0.01	0.7172	3.5033	1.2024	2.9564	0.2348	−0.2348	0.7875
	τ = 0.1	0.7844	3.4329	1.3081	2.8596	0.2200	−0.2094	0.7970
	τ = 0.2	0.8513	3.3555	1.4057	2.7521	0.1985	−0.1875	0.8043
	τ = 1	1.1296	2.7447	1.7896	2.039	0.1167	−0.1046	0.8222
	τ = 2	1.1889	2.1613	1.8622	1.4477	0.0766	−0.0646	0.8242
	τ = 5	1.0540	1.2569	1.6282	0.6538	0.0334	−0.0237	0.8224
τ = 1, ω = 0.5, ε = 0.5	RC = 0.0	0.5000	0.0000	0.5000	0.0000	0.0000	0.0000	0.7500
	RC = 0.01	0.5009	0.0029	0.5022	0.0016	0.0002	−0.0002	0.7502
	RC = 0.1	0.5094	0.0288	0.5218	0.0162	0.0026	−0.0023	0.7524
	RC = 1.0	0.5914	0.2842	0.7019	0.1701	0.0229	−0.0209	0.7701
	RC = 10.0	1.1296	2.7447	1.7896	2.039	0.1167	−0.1046	0.8222
	RC = 40.0	1.9313	10.829	3.4985	9.0987	0.192	−0.1724	0.8401
	RC = 100.0	2.7199	26.8735	5.3471	23.958	0.2161	−0.1925	0.8451
τ = 1, RC = 10, ε = 0.5	ω = 0.0	1.4444	2.7223	2.1986	1.9202	0.0888	−0.0755	0.8246
	ω = 0.5	1.1296	2.7447	1.7896	2.039	0.1167	−0.1046	0.8222
	ω = 1.0	0.6245	2.752	1.062	2.2742	0.2253	−0.2157	0.7851
τ = 1, RC = 10, ω = 0.5	ε = 0.1	1.3339	0.5762	1.5624	0.3389	0.0164	−0.0119	0.7976
	ε = 0.5	1.1296	2.7447	1.7896	2.039	0.1167	−0.1046	0.8222
	ε = 1.0	0.8889	5.6748	1.7718	4.6977	0.2023	−0.1871	0.8324

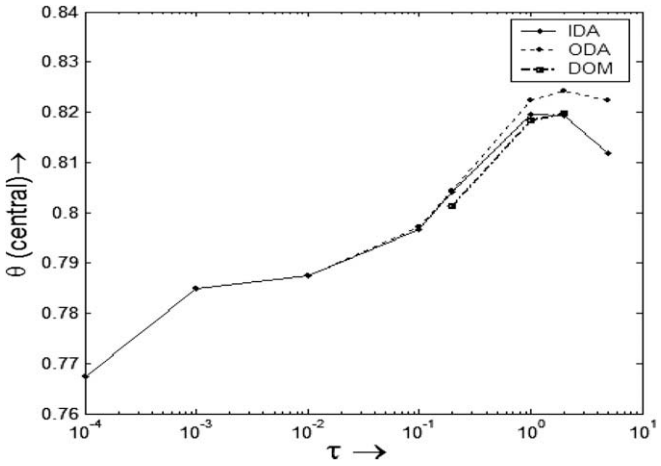

Fig. 5. The variation of central node temperature at different opacities for RC = 10, ω = 0.5, ε = 0.5.

This feature is not noticed during the simulation of DOM [20] and ODA.

The CCR models for the non-homogeneous boundary conditions, are not reported by many researchers. So, Fig. 7 is presented which shows the temperature variation along the *x*-direction at the symmetry line *Y* = 0.5 for different RC values. The results are compared with DOM [20] favorably. A steeper temperature gradient is observed very close to the hot and cold wall for higher RC value (100). This signifies the radiation dominant over conduction for higher RC values (Tables 2 and 3).

4.2.3. Effect of single scattering albedo (ω)

Fig. 8 compares the isotherms for non-scattering and purely scattering medium. For non-scattering medium, the domain core temperature is more as compared to purely scattering medium (Tables 2 and 3). But, the conductive heat flux decreases evidently for purely scattering medium. The bent isotherms for purely scattering (i.e. ω = 1) also reflects the radiative heat transfer dominant over conductive heat transfer.

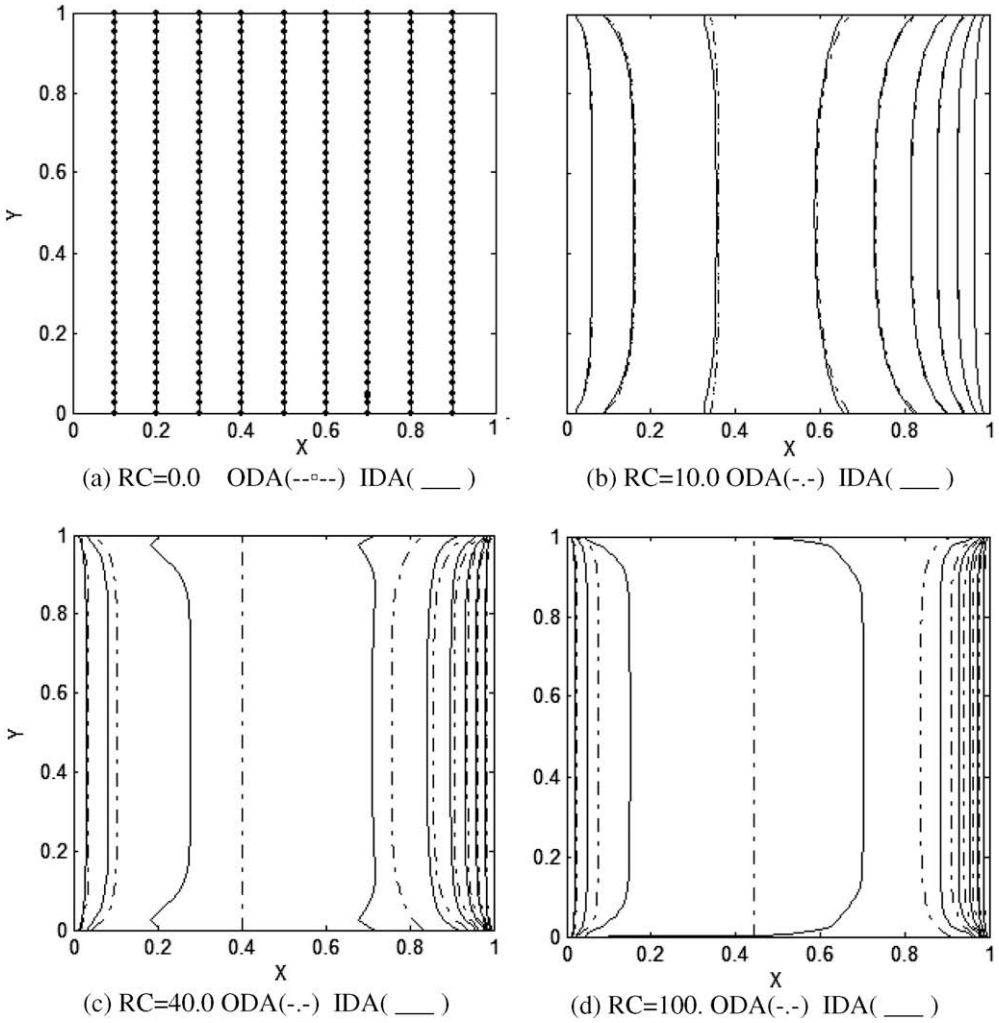

Fig. 6. Comparison of isotherms of IDA with ODA for different values of RC. (a) RC = 0, (b) RC = 10, (c) RC = 40, (d) RC=100, when $\tau = 1$, $\omega = 0.5$, $\varepsilon = 0.5$.

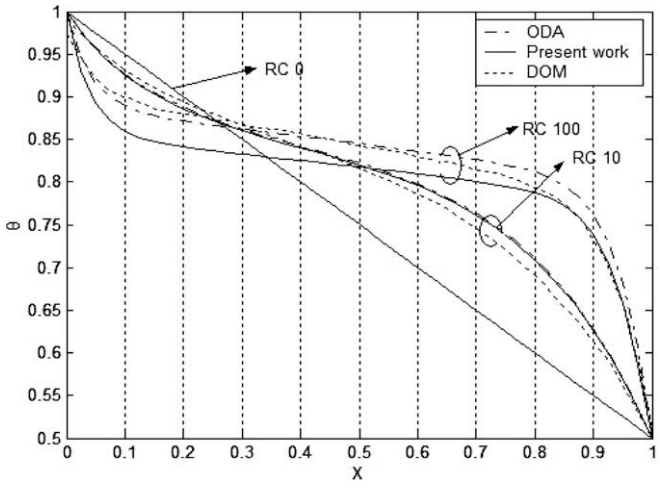

Fig. 7. Variation of mid-plane temperature ($Y = 0.5$) and comparison when, $\tau = 1$, $\omega = 0.5$, $\varepsilon = 0.5$.

4.2.4. Effect of gray surface emissivity (ε)

The boundary walls are gray, black/non-black, diffuse and opaque surfaces. As it is displayed in Fig. 9(a) the isotherms are straight in the domain but slightly bends near the wall because of diffuse emission of some radiance, this behavior predicts the nature of isotherms for a reflector wall. From Fig. 9(a) and Tables 2 and 3, it is observed that for lower emissivity conduction mode predominates near the isothermal walls, as the snug isotherms indicate this behavior. But in the core the radiative transfer prevails.

When the emissivity of the wall increases the reflection behavior diminishes that leads to acute bending of isotherms gradually as these march from core to the insulated wall Fig. 9(b). The conduction mode near cold wall prevails as compared to hot wall, but radiance improves drastically which also improves the core temperature and central node temperature significantly.

4.2.5. Validation with experimental work

The schematic diagrams of the cavity and experimental set up are delineated in Fig. 3. During numerical simulation of experimental conditions of the present model, the low-scattering gray gas ($\omega = 0.001$) with low-extinction co-efficient ($\beta = 0.3$) and the insulated walls emissivity ($\varepsilon = 0.96$) and the active walls emissivity ($\varepsilon = 0.05$) are considered with opacity $\tau = 0.003$ and RC = 0.89. For calculation of RC $= \frac{\sigma T_H^3 L}{k}$ value, the characteristic length of the cavity is taken as 0.01 m, hot wall temperature is 328 K and thermal conductivity of air is 22.48e−03 W/m K. The wall emissivity values for polished aluminum and bakelite are taken from standard texts[31] as 0.05 and 0.96, respectively. The extinction coefficient of air is taken from results of Baek et al. [26] as 0.3.

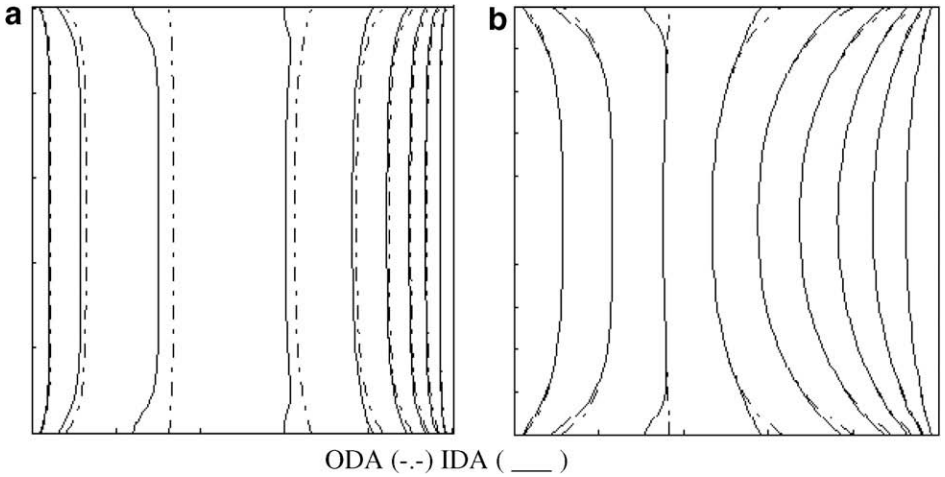

Fig. 8. Comparison of isotherm pattern of IDA and ODA with variation of single scattering albedo. (a) $\omega = 0$, (b) $\omega = 1$ when RC = 10, $\tau = 1$, $\varepsilon = 0.5$.

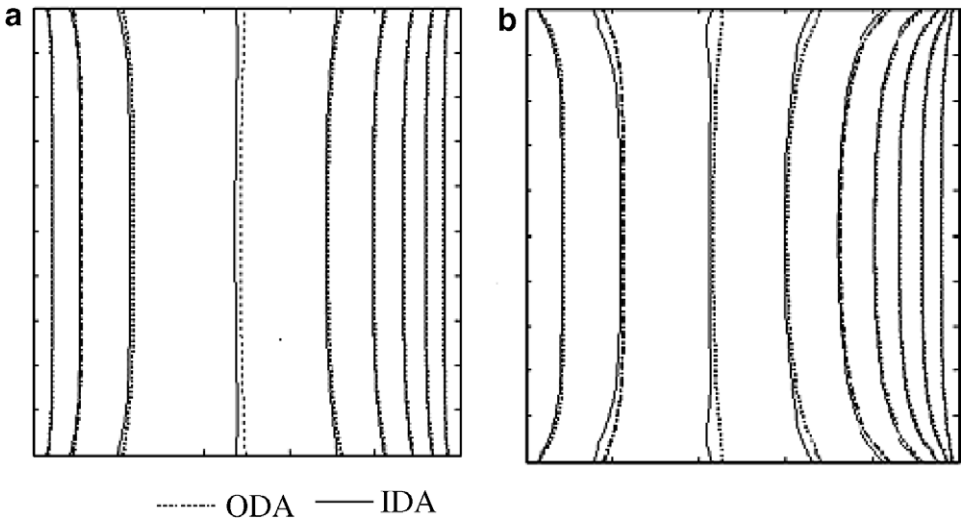

Fig. 9. Comparison of isotherm pattern of IDA and ODA with variation of surface emissivity. (a) $\varepsilon = 0.1$, (b) $\varepsilon = 1$ when RC = 10, $\tau = 1$, $\omega = 0.5$.

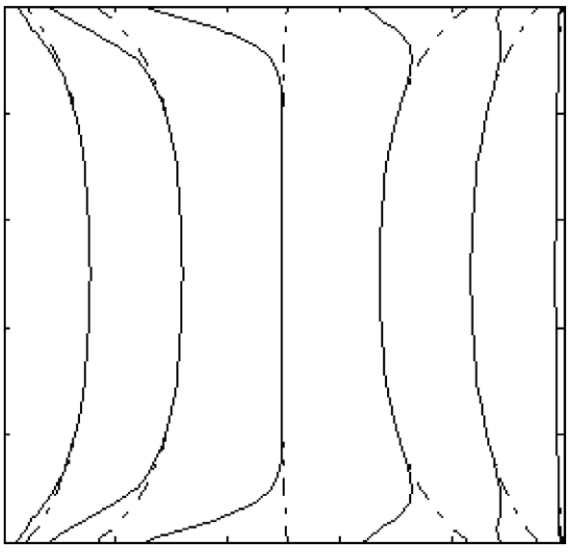

Fig. 10. Comparison of IDA (-) and ODA (--) isotherm for experimental setup.

The CCR model is simulated; the ODA and IDA isotherms are compared and depicted in Fig. 10. The isotherms bend at the adiabatic surfaces because of impinging radiative fluxes from the high emissive walls, but the isotherms remains straight at the central portion of the domain signifies non-scattering behaviors of the gray gas Fig. 10. As both top and bottom walls are insulated the walls are extremely heated, for this reason the isotherms bend near the insulated walls only. The clustering of isotherms near the cold wall depicts enhanced conduction mode of heat transfer. The small size of domain inhibits the dynamics of fluid medium due to density gradients, for which it is as a conduction–radiation phenomenon [1]. The comparison of isotherm patterns of IDA with interferogram is depicted in Fig. 12, and the detailed output after post processing of the model is shown in Table 4.

Table 4
Experimental simulation for hot wall at 55 °C and cold wall at 35 °C

QCH	QRH	QCC	QRC	QCb	QRb	θ_{center}
0.0838	0.2112	0.1087	0.1827	0.0071	−0.0063	0.9693

Aluminum metal ($\varepsilon = 0.05$) and insulated walls ($\varepsilon = 0.96$) ($\tau = 0.003$, RC = 0.89, $\omega = 0.001$, $\beta = 0.3$).
(RC = 0.89, $\tau = 0.003$, $\omega = 0.001$, $\varepsilon_{H,C} = 0.05$, $\varepsilon_{b,t} = 0.96$, $\theta_H = 1$ and $\theta_C = 0.939$).

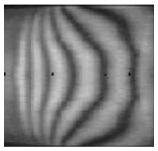

Fig. 11. Interferogram captured by Mach–Zehnder interferometer.

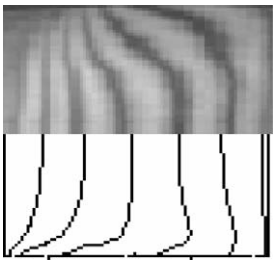

Fig. 12. Comparison of IDA isotherm and interferogram.

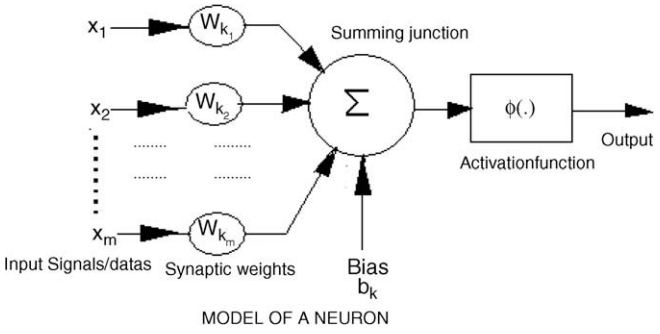

Fig. 13. Model of a neuron.

The comparison of isotherm patterns for ODA and IDA signifies the more departure of isotherms nearing to the insulated wall in Fig. 10. The bending of isotherms at the proximity of the wall is also depicted in the interferogram captured by the Mach–Zehnder interferometer Fig. 11. The natural trend of isotherm pattern shown in Fig. 11 interferograms is found similar with that of the IDA isotherms in Fig. 10. Therefore, the IDA with NFDM concept of modeling is realistic. Furthermore, the authors found difficulty in simulation of this case by hybrid method [22] as the overall opacity of this cavity (0.003) is very small. The output result tables pertaining to IDA, ODA and experimental cavity are presented for bench marking the solution.

5. Conclusion

The present CCR model is simulated by applying the NFDM concept for the calculation of view factor, solid angle and average optical thickness of rays. The present model has capability to simulate the physical situation like the air filled cavity, as most of the CCR models break down during simulation of lower overall opacity (<0.1) medium[2]. The special features of this CCR model are outlined as follows.

1. It is versatile and robust in producing results, i.e. for overall opacity 0.0001 to 10, scattering albedo 0 to 1, surface emissivity any value just above zero to one, and radiation–conduction parameter from 0 to as high as 100.
2. The limitation of this model is its non-responding nature for reflecting boundary (i.e. for surface emissivity zero),but submits results for very low emissivity (0.1) which is CPU intensive.
3. It submits result from very low opacity to very high opacity without much fluctuation or oscillation in the output values, although the computational time is substantially significant for both extreme values. So, it is advisable to implement P_1 model for higher opacity (1–10) for the purpose of computational economy. For lower opacity range (<1) the IDA implementation is more persuasive for its accuracy and boundary wall effects.
4. The properties of participating gasses can be estimated by matching the interferogram with the present radiation model output isotherm patterns for a specific set of radiative properties values.

Acknowledgement

The financial assistance provided by the DST, India for the Mach–Zehnder interferometer set up is gratefully acknowledged.

Appendix. Models of a neuron and its application for development of IDA

A neuron is an information processing unit that is fundamental to the operation of a neural network. The model of a neuron, which forms the basis for designing neural networks, is explained and shown in Fig. 13.

Here, three basic elements of the neuronal model are identified:

1. A set of synapses or connecting links, each of which is characterized by a weight or strength of its own. Specifically, a signal (temperature or irradiation) x_j at the input of the synapse j connected to neuron k is multiplied by the synaptic weight (exponential decay of intensity and solid angle) w_{kj}. It is important to make a note of the manner in which the subscripts of the synaptic weight w_{kj} are written. The first subscript refers to the neuron in question (i.e. a node under consideration) and the second subscript (i.e. sub-node) refers to the input end of the synapse to which the weight refers.
2. An adder for summing the input signals, weighted by the respective synapses of the neuron; the operations described here constitutes a linear combiner.
3. An activation function for limiting the amplitude of the output of a neuron. The activation function is also referred to as a squashing function in that it squashes (limits) the permissible amplitude range of the output signal to some finite value. In this radiation modeling activation function is implemented as improved values are just the values after considering the effect of all sub-nodes on a particular node.

In this formulation no bias is used, as P_1 approximation result is some how numerically unbiased for optically thin medium and IDA formulation just considers the geometrical position of each nodes lying on the domain.

In mathematical terms, we may describe a neuron k by writing the following pair of equations:

$$u_k = \sum_{j=1}^{m} w_{kj} x_j \tag{35}$$

and

$$y_k = \varphi(u_k + b_k), \tag{36}$$

where x_1, x_2, x_3, ..., x_m are the input signals.
w_{k1}, w_{k2}, w_{k3}, ..., w_{km} are the synaptic weights of neuron k.
u_k is the linear combiner output due to the input signals.
b_k is the bias; and $\varphi(.)$ is the activation function.
y_k is the output signal of the neuron.

References

[1] K.A.R. Ismail, S.S. Carlos, Non-gray radiative convective conductive modeling of a double glass window with a cavity filled with a mixture of absorbing gases, Int. J. Heat Mass Transfer 49 (2006) 2972–2983.
[2] M.M. Razzaque, J.R. Howell, D.E. Klein, Coupled radiative and conductive heat transfer in a two-dimensional rectangular enclosure with gray participating media using finite elements, J. Heat Transfer 106 (1984) 613–619.
[3] T.Y. Kim, S.W. Baek, Analysis of combined conductive and radiative heat transfer in a two-dimensional rectangular enclosure using discrete ordinate method, Int. J. Heat Mass Transfer 34 (1991) 2265–2273.
[4] M. Sakami, A. Charette, V.L. Dez, Application of the discrete ordinates method to combined conductive and radiative heat transfer in a two-dimensional complex geometry, J. Quant. Spectrosc. Radiat. Transfer 56 (1996) 517–523.
[5] W.W. Yuen, E.E. Takara, Analysis of combined conductive–radiative heat transfer in a two-dimensional rectangular enclosure with a gray medium, J. Heat Transfer 110 (1988) 468–474.
[6] S.C. Mishra, N. Kaur, H.K. Roy, The DOM approach to the collapsed dimension method for solving radiative transport problems with participating media, Int. J. Heat Mass Transfer 49 (2006) 30–41.
[7] T.M. Shih, Y.N. Chen, A discretized-intensity method proposed for two-dimensional systems enclosing radiative and conductive media, Numer. Heat Transfer 6 (1983) 117–134.
[8] P.J. Coelho, M.G. Carvalho, A conservative formulation of the discrete transfer method, J. Heat Transfer 119 (1997) 118–128.
[9] G.D. Raithby, E.H. Chui, A finite-volume method for predicting a radiant heat transfer in enclosures with participating media, J. Heat Transfer 112 (1990) 415–423.
[10] M.F. Modest, The modified differential approximation for radiative transfer in general three-dimensional media, J. Thermophys. Heat Transfer 3 (1989) 283–288.
[11] D.B. Olfe, Radiative equilibrium of a gray medium bounded by non-isothermal walls, Prog. Astronaut. Aeronaut. 23 (1970) 295–317.
[12] M. Sakami, A. El Kasmi, A. Charette, Analysis of radiative heat transfer in complex two-dimensional enclosures with obstacles using the modified discrete ordinate method, J. Heat Transfer 123 (2001) 892–900.
[13] M. Sakami, A. Charette, Application of a modified discrete ordinates method to two-dimensional enclosures of irregular geometry, J. Quant. Spectrosc. Radiat. Transfer 64 (2000) 275–298.
[14] A.C. Ratzel III., J.R. Howell, Two-dimensional radiation in absorbing–emitting media using the P–N approximation, J. Heat Transfer 105 (1983) 333–340.
[15] Y. Bayazitoglu, J. Higenyi, Higher order differential equations of radiative transfer P-3 approximation, AIAA J. 17 (1979) 424–431.
[16] Documentation of Fluent. Inc.
[17] S. Maruyama, T. Aihara, Radiation heat transfer of arbitrary three-dimensional absorbing, emitting and scattering media and specular and diffuse surfaces, J. Heat Transfer 119 (1997) 129–136.
[18] D.B. Olfe, Application of modified differential approximation to radiative transfer in a gray medium between concentric cylinders and spheres, J. Quant. Spectrosc. Radiat. Transfer 8 (1968) 899–907.
[19] M.F. Modest, The improved differential approximation for radiative transfer in multidimensional media, J. Heat Transfer 112 (1990) 819–821.
[20] Mahapatra, S.B. Mahapatra, Numerical modeling of combined conductive and radiative heat transfer within square enclosure using discrete ordinate method, Heat Mass Transfer 40 (2004) 533–538.
[21] W.A. Fiveland, Discrete ordinate solutions of the radiative transport equation for rectangular enclosures, J. Heat Transfer 106 (1984) 699–706.
[22] S.K. Mahapatra, B.K. Dandapat, A. Sarkar, Analysis of combined conduction and radiation heat transfer in presence of participating medium by the development of hybrid method, J. Quant. Spectrosc. Radiat. Transfer 102 (2006) 277–292.
[23] F. Liu, J. Swithenbank, E.S. Garbett, The boundary condition of the P_N-approximation used to solve the radiative transfer equation, Int. J. Heat Mass Transfer 35 (1992) 2043–2052.
[24] McClatchey et al., AFCRL atmospheric absorption line parameters compilation, Environmental Research Papers, 1973.
[25] A.T. Modak, Thermal radiation from pool fires, Combust. Flame 29 (1977) 177–192.
[26] C.Y. Han, S.W. Baek, Natural convection phenomena affected by radiation in concentric and eccentric horizontal cylindrical annuli, Numer. Heat Transfer A 36 (1999) 473–488.
[27] T.H. Kuehn, R.J. Goldstein, An experimental and theoretical study of natural convection in the annulus between horizontal concentric cylinders, J. Fluid Mech. 74 (1976) 695–719.
[28] C.S. Chen, J.D. Bird, Alignment technique for the Mach–Zehnder interferometer using lasers, J. Phys. E Sci. Instrum. 4 (1971) 157–158.
[29] Simon Haykin, Neural Network, second ed., Pearson, 2004, pp. 10–15.
[30] R.K. Mishra, P.S. Hall, NFDTD concept, IEEE Trans. Neural Netw. 16 (2005) 484–490.
[31] M.F. Modest, Radiative Transfer, Mc-Graw Hill, Singapore, 1993.